Supporting Information

Structure, photoluminescence, and magnetic properties of a Mn(II)-based metal-organic framework

Hyojin Kim,†[a] Sunhwi Eom,†[a] Sora Park, †[a] Dong Won Kang,[a] Mengmeng Wang,[b] Youngseo Kim,[a] Sungnam Park,[a] Wei Shi,*[b] and Chang Seop Hong *[a]

[a]*Department of Chemistry, Korea University, Seoul 02841, Republic of Korea.*
[b]*Department of Chemistry, Nankai University, 94 Weijin Road, Tianjin 300071, P. R. China.*

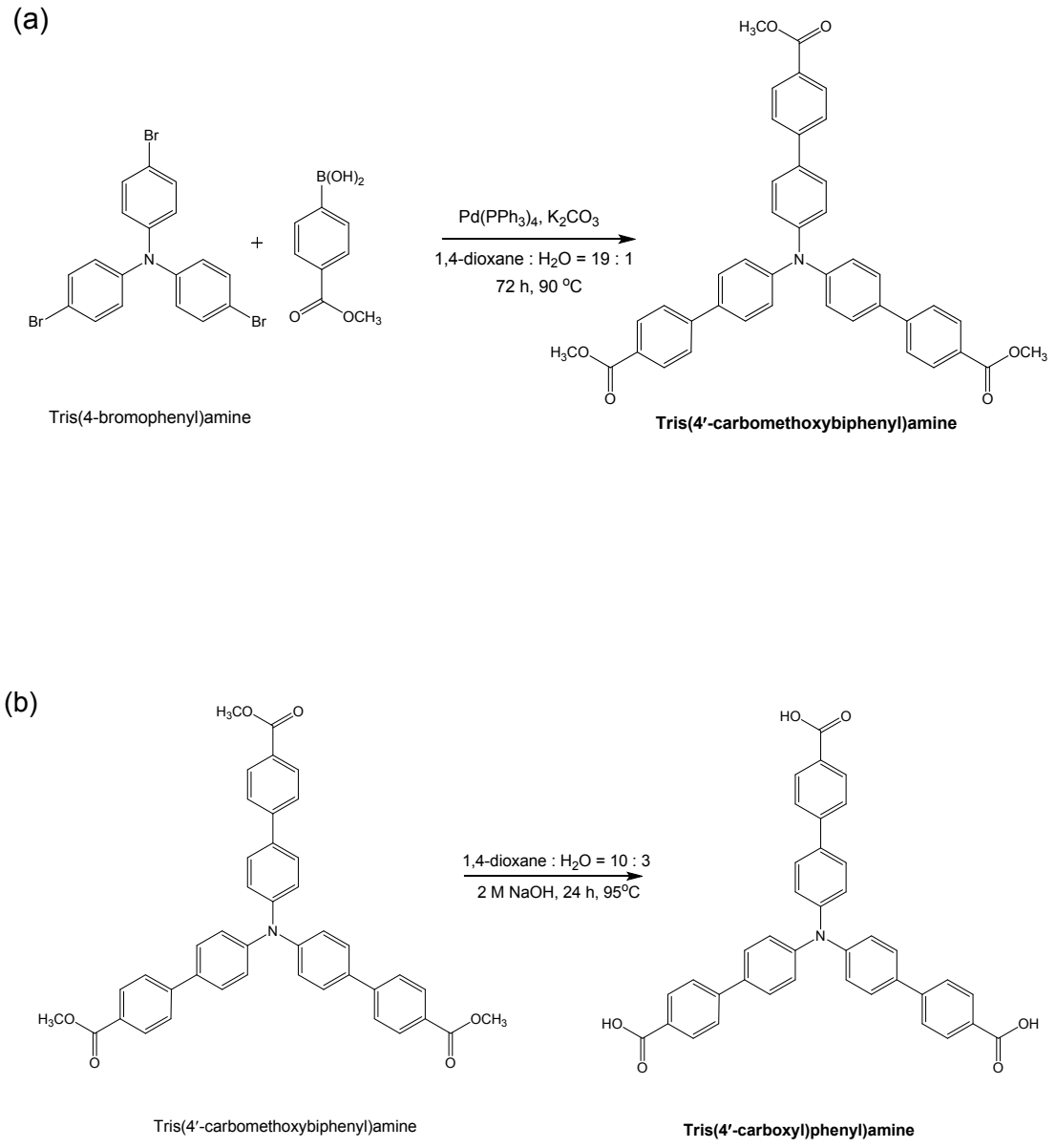

Scheme S1. Schematic illustrations for synthesis of (a) tris(4′-carbomethoxybiphenyl)amine and (b) tris((4-carboxyl)phenyl)amine (H_3L).

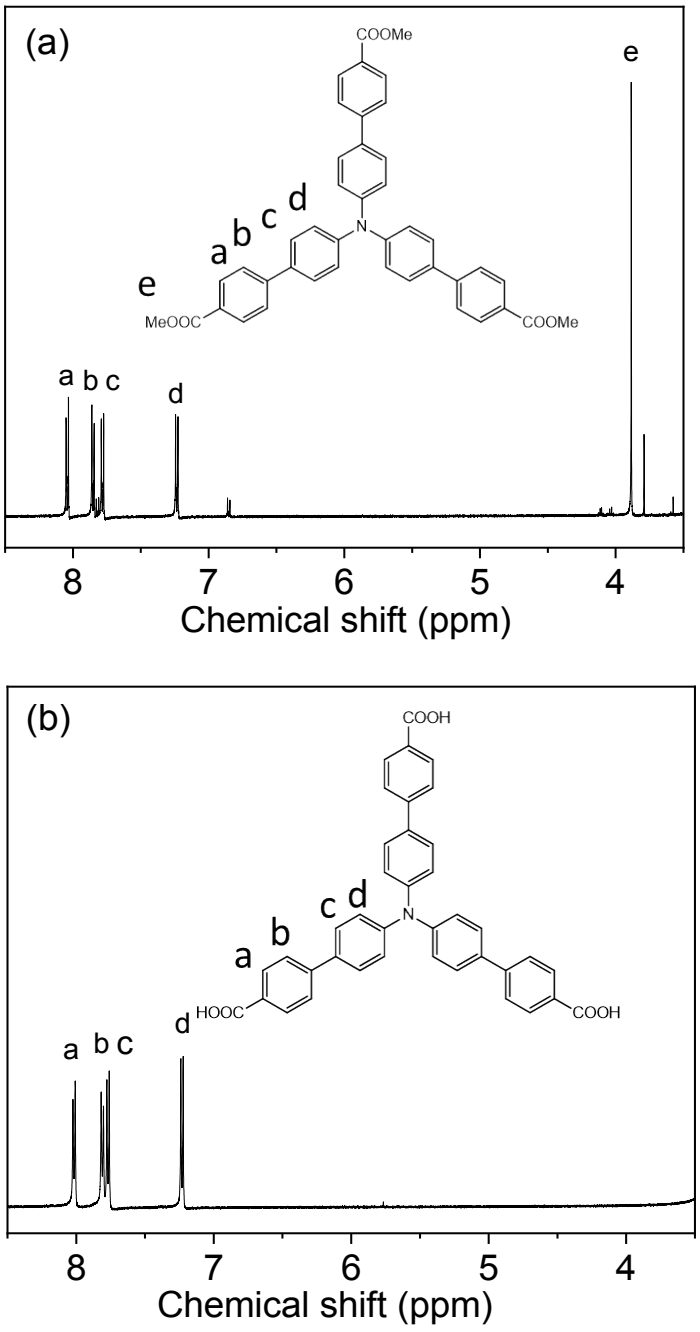

Fig. S1. ^{1}H NMR of (a) tris(4′-carbomethoxybiphenyl)amine and (b) tris((4-carboxyl)phenyl)amine (H_3L) (NMR solvent: DMSO).

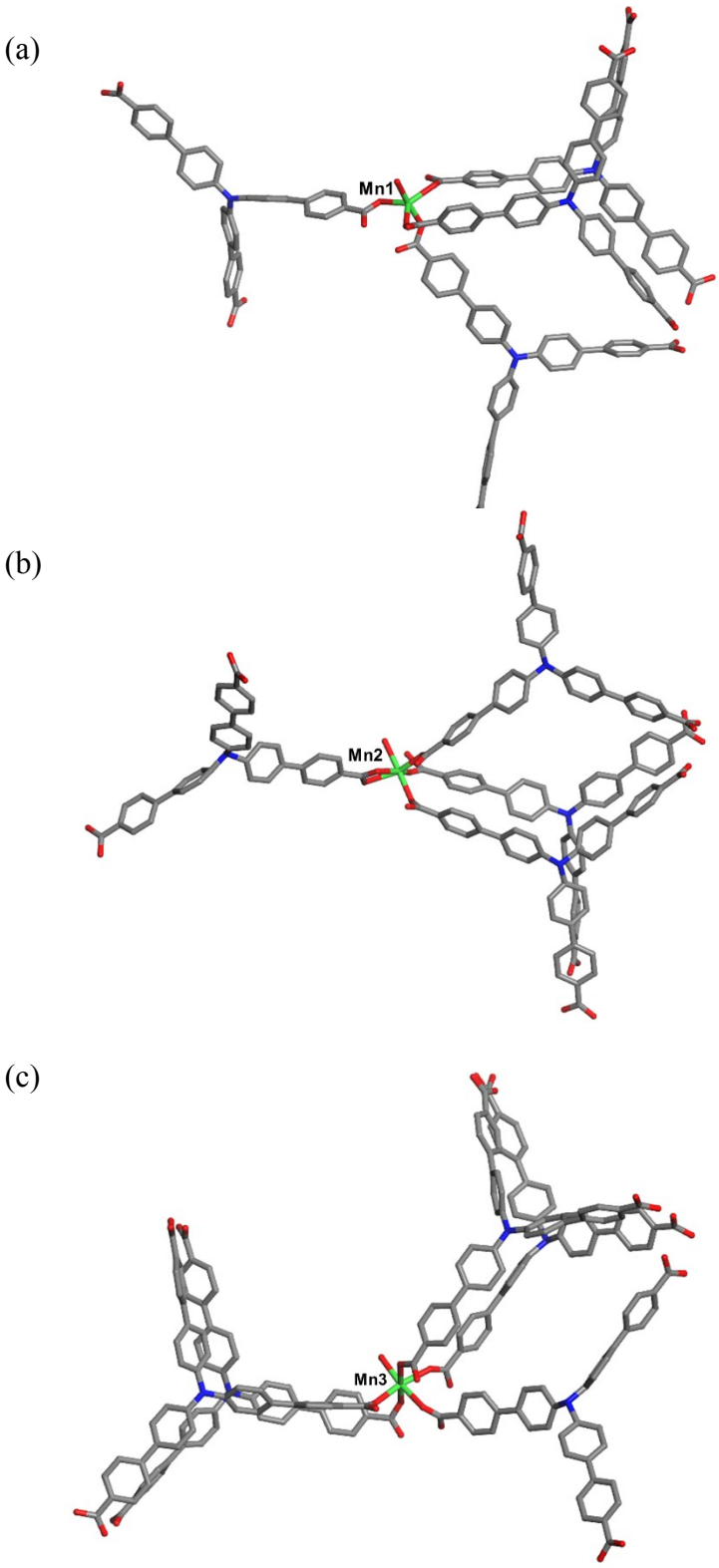

Fig. S2. Coordination structures of (a) Mn1 (trigonal bipyramidal), (b) Mn2 (distorted octahedral), and (c) Mn3 (distorted octahedral).

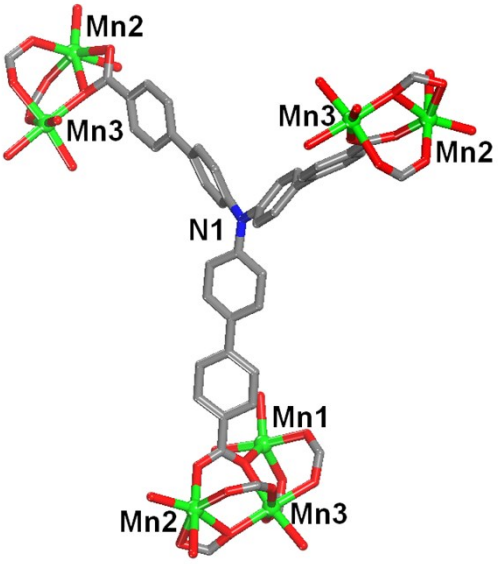

(a)

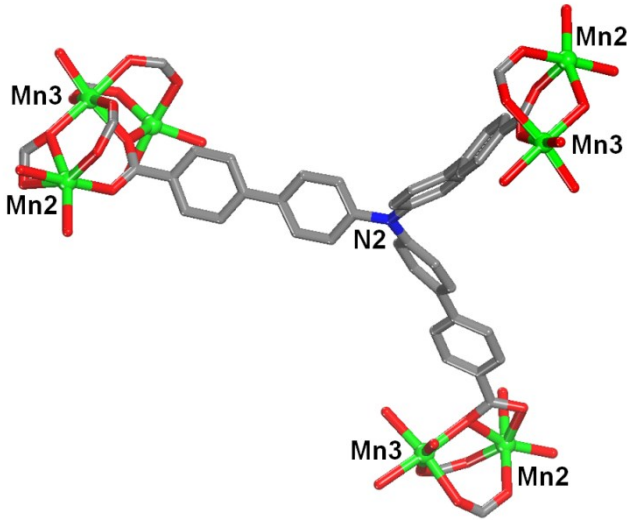

(b)

Fig. S3. Binding modes of Mn ions by the L^{3-} ligand.

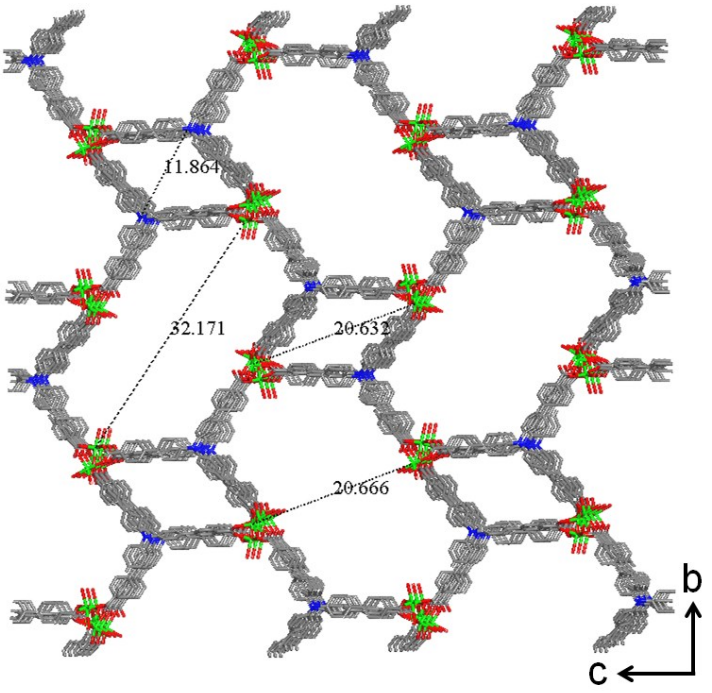

(a)

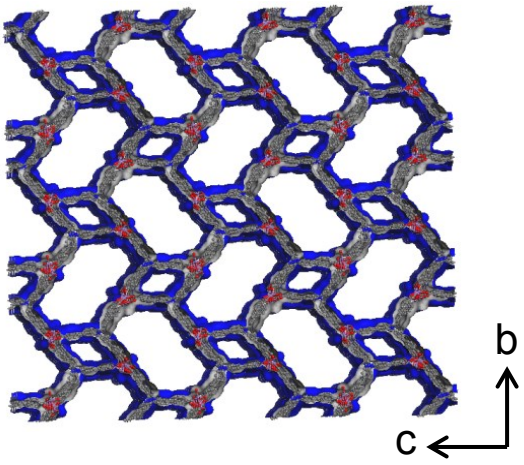

(b)

Fig. S4. (a) Extended structure of **1** in the *bc* plane showong 4- and 6-membered rings. The channel sizes of the 4- and 6-membered rings correspond to 11.9 x 20.6 $Å^2$ and 20.7 x 32.2 $Å^2$. (b) Connolly surface of **1** with a probe radius of 1 Å.

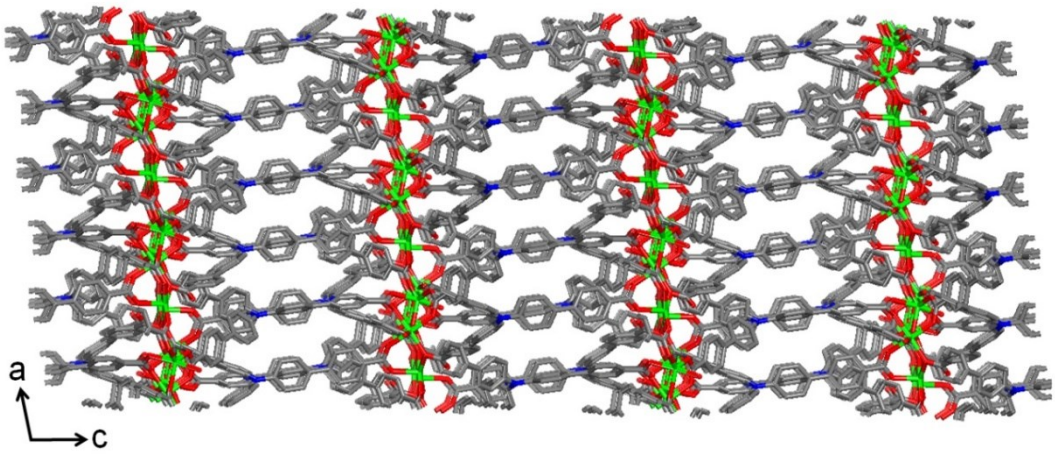

Fig. S5. Extended structure of **1** in the ac plane.

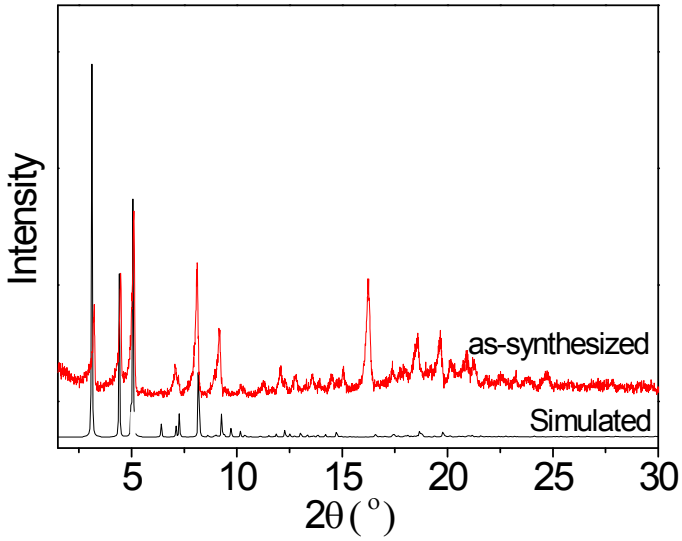

Fig. S6. PXRD data of **1**. The profile coincided with the simulated pattern. The discrepancy could be caused by preferred orientation and the lattice solvent molecules that are not considered in the simulated pattern.

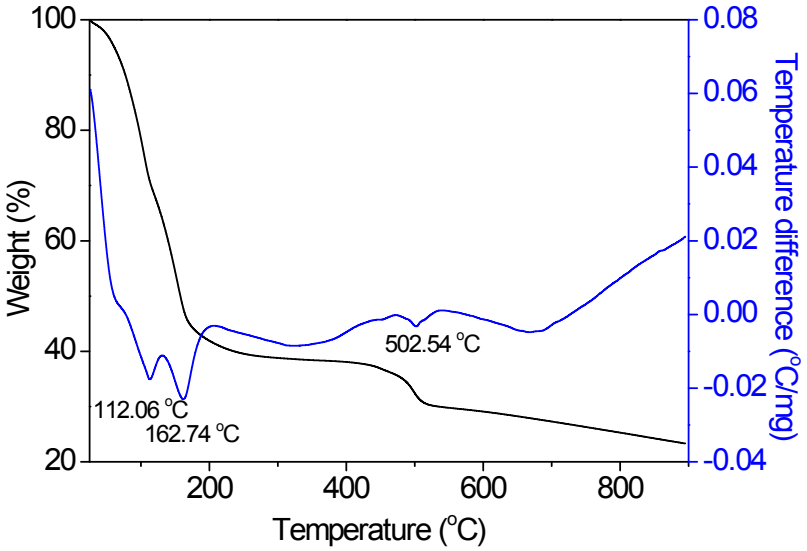

Fig. S7. TGA and DSC curves of **1**. TGA and DSC were conducted to determine the thermal stability of **1**. The initial mass decrease below 200 °C is due to the weight loss of solvent molecules (H_2O and DEF) from the framework. A weight loss observed at about 500 °C is ascribed to the framework decomposition of **1**.

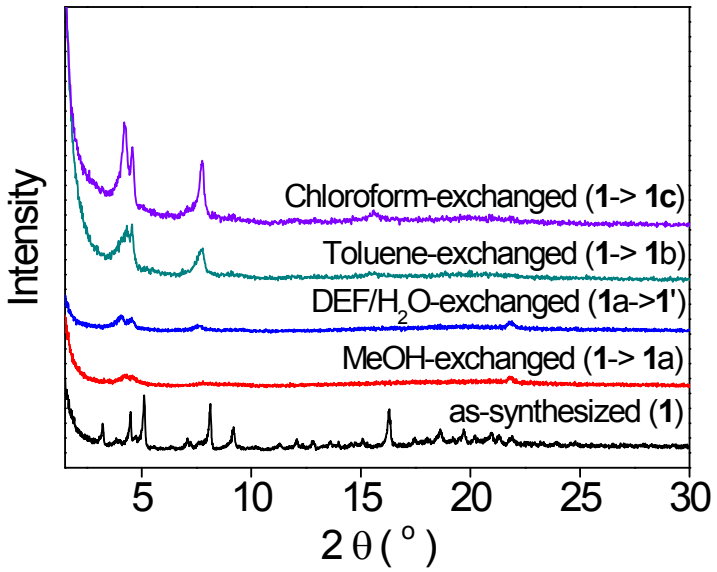

Fig. S8. PXRD data of as-synthesized (**1**), MeOH-exchanged (**1**a), and DEF/H_2O-exchanged (**1**'), Toluene-exchanged (**1**b), Chloroform-exchanged (**1**c) after the solvent exchange process.

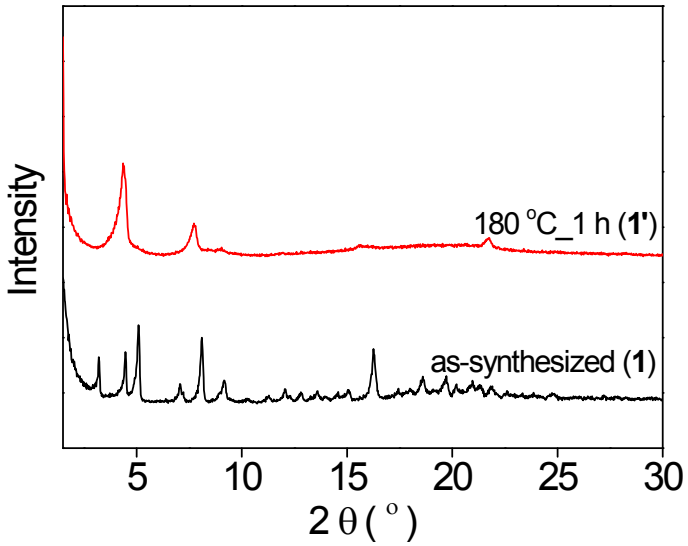

Fig. S9. PXRD data of as-synthesized **1** and **1**' treated in vacuum at 180 °C for 1 h.

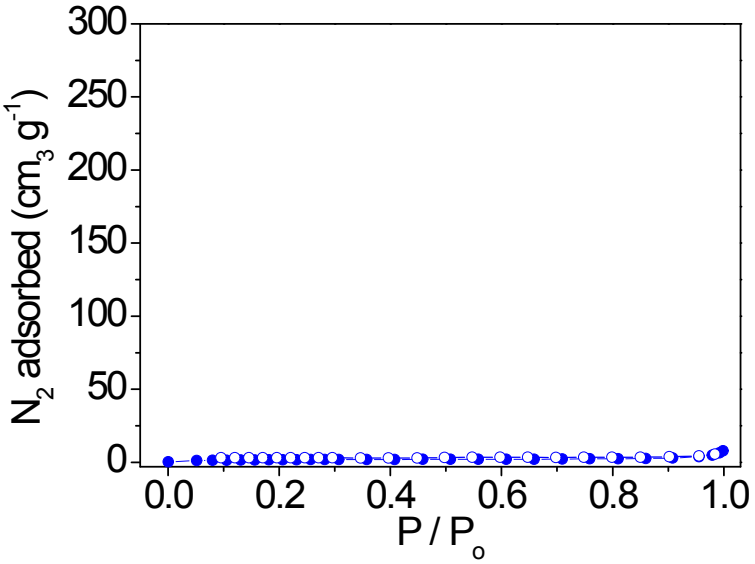

Fig. S10. N_2 isotherm of the activated **1** at 77 K, implying that direct activation of the sample results in structural collapse.

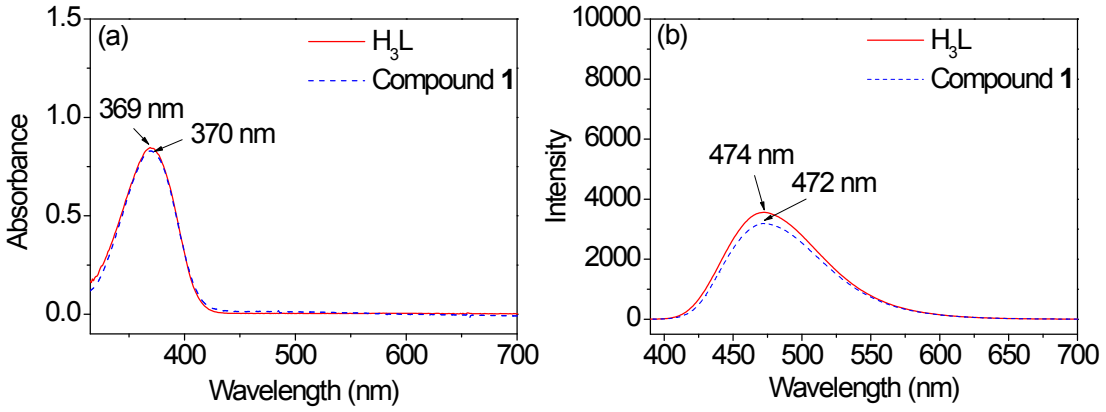

Fig. S11. (a) UV-vis data of H_3L (line) and **1** (dashed line) in DEF. (b) PL data of H_3L (line) and **1** (dashed line) upon excitation at 369 nm.

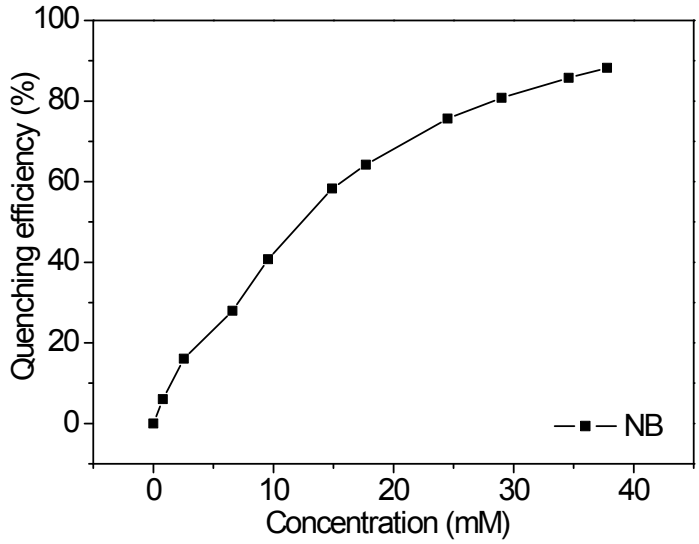

Fig. S12. Quenching efficiency of **1** as a function of the concentration of NB.

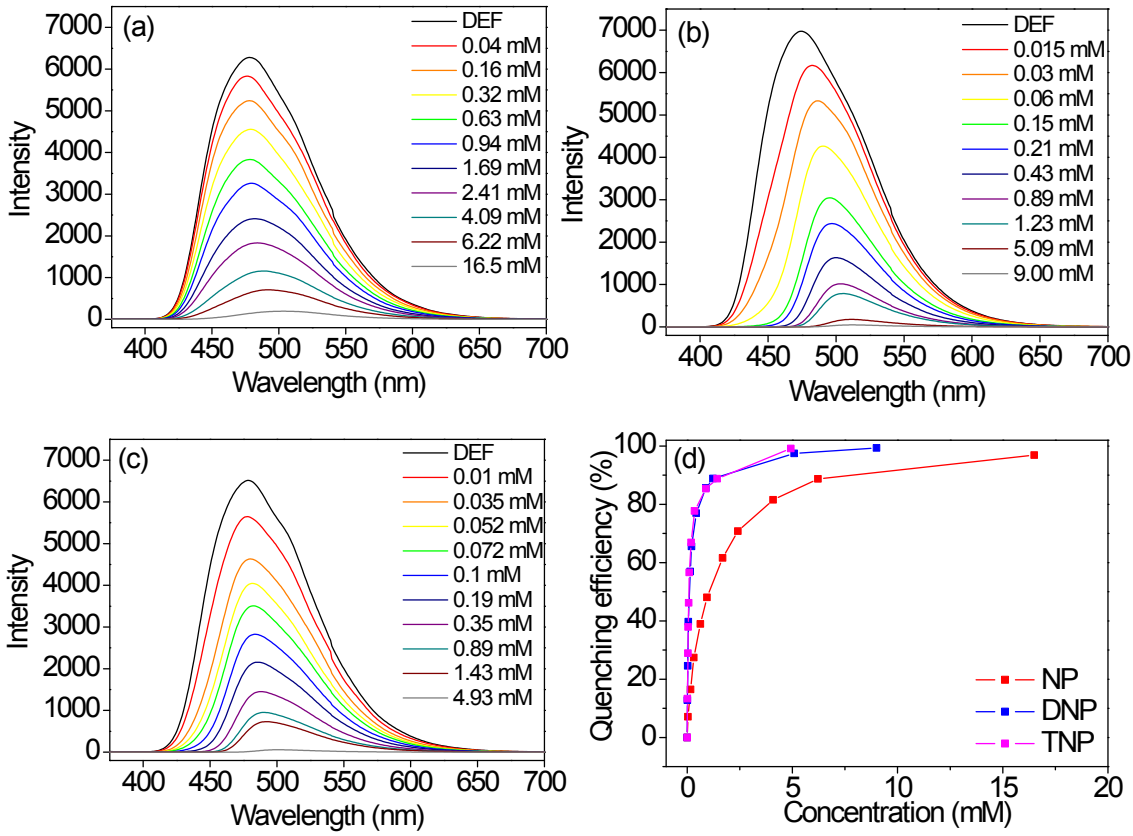

Fig. S13. Photoluminescence data of **1** after addition of (a) NP, (b) DNP, and (c) TNP with different concentrations. (d) Quenching efficiency of **1** for NP, DNP, and TNP.

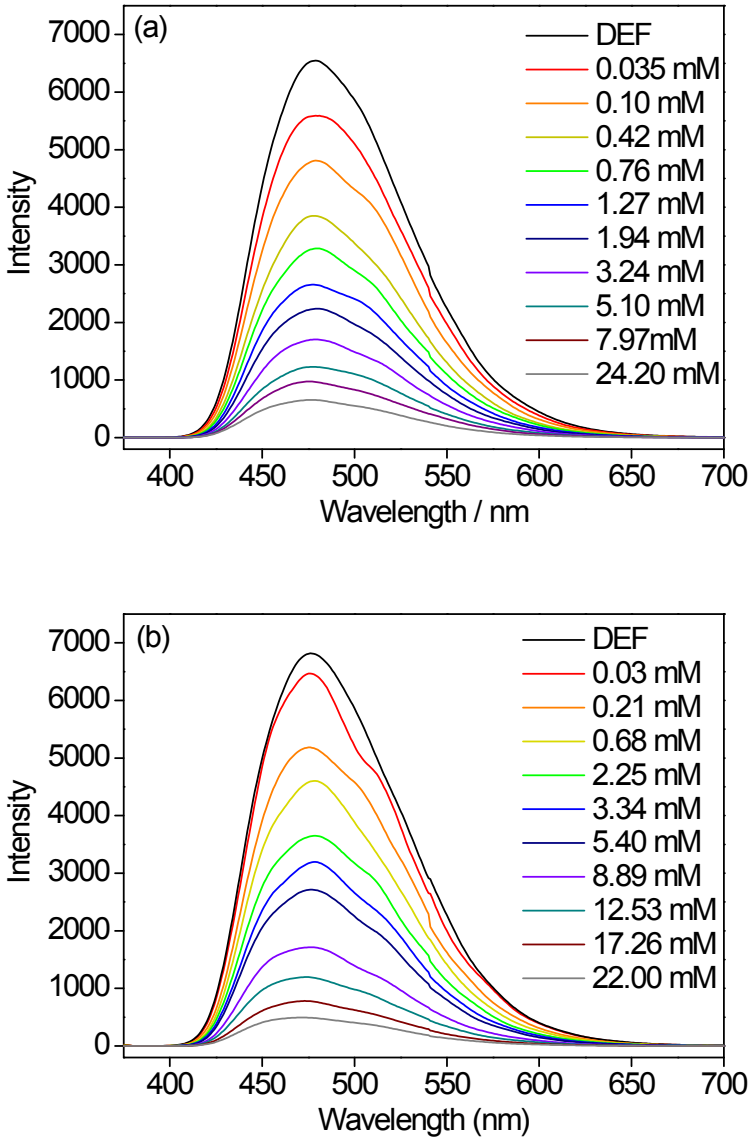

Fig. S14. Photoluminescence data of **1** after the addition of (a) NT and (b) DNT.

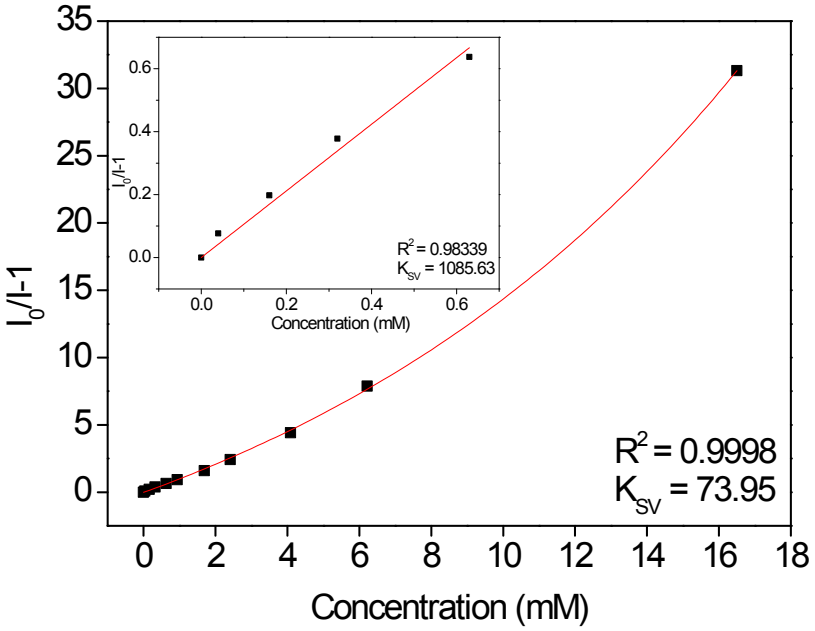

Fig. S15. The nonlinear Stern-Volmer plot of **1** at 25 °C as a function of the concentration of NP in DEF. The solid curve is the fitted results by an exponential quenching formula, $I_0/I = Aexp(k[M]) + B$. A, B, and k were determined to be 13.12, -12.14, and 0.074 in the concentration region. The inset shows the Stern-Volmer plot in the low concentration range. The solid line in the inset is the fitted result by the Stern-Volmer equation, $I_0/I = (1.09 \times 10^3)[M] + 1$.

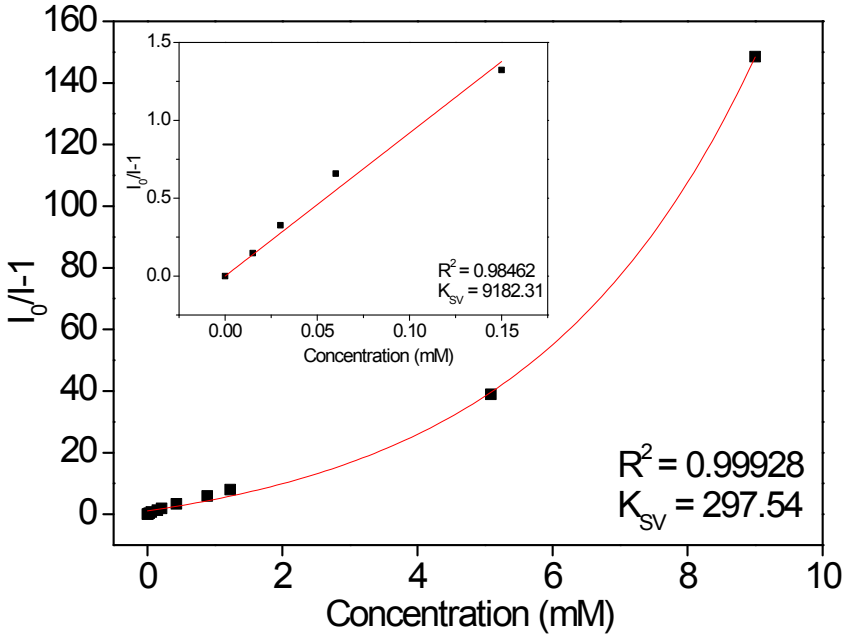

Fig. S16. The nonlinear Stern-Volmer plot of **1** at 25 °C as a function of the concentration of DNP in DEF. The solid curve is the fitted results by an exponential quenching formula, $I_0/I = Aexp(k[M]) + B$. A, B, and k were determined to be 10.87, -8.78, and 0.30 in the concentration region. The inset shows the Stern-Volmer plot in the low concentration range. The solid line in the inset is the fitted result by the Stern-Volmer equation, $I_0/I = (9.18 \times 10^3)[M] + 1$.

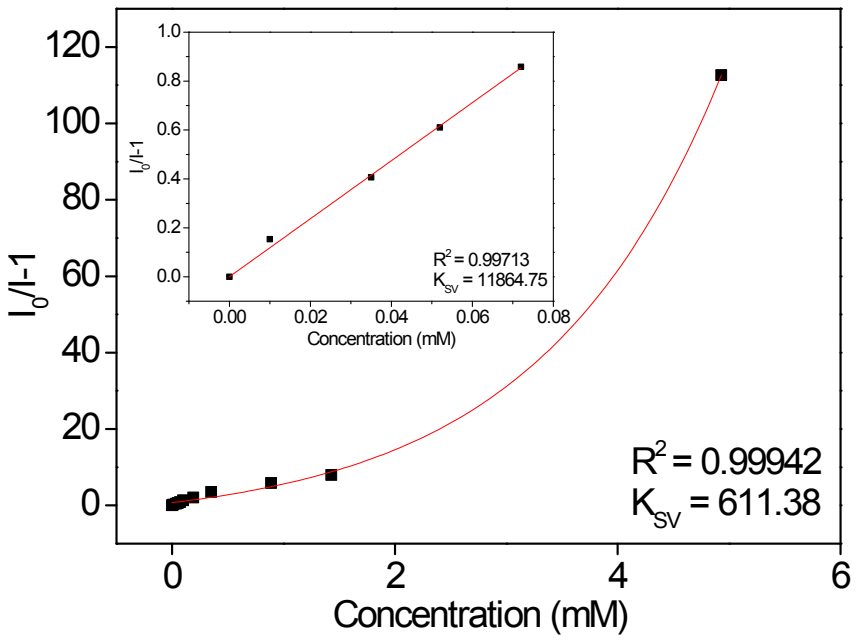

Fig. S17. The nonlinear Stern-Volmer plot of **1** at 25 °C as a function of the concentration of TNP in DEF. The solid curve is the fitted results by an exponential quenching formula, $I_0/I = Aexp(k[M]) + B$. A, B, and k were determined to be 5.78, -4.05, and 0.61 in the concentration region. The inset shows the Stern-Volmer plot in the low concentration range. The solid line in the inset is the fitted result by the Stern-Volmer equation, $I_0/I = (1.19 \times 10^4)[M] + 1$.

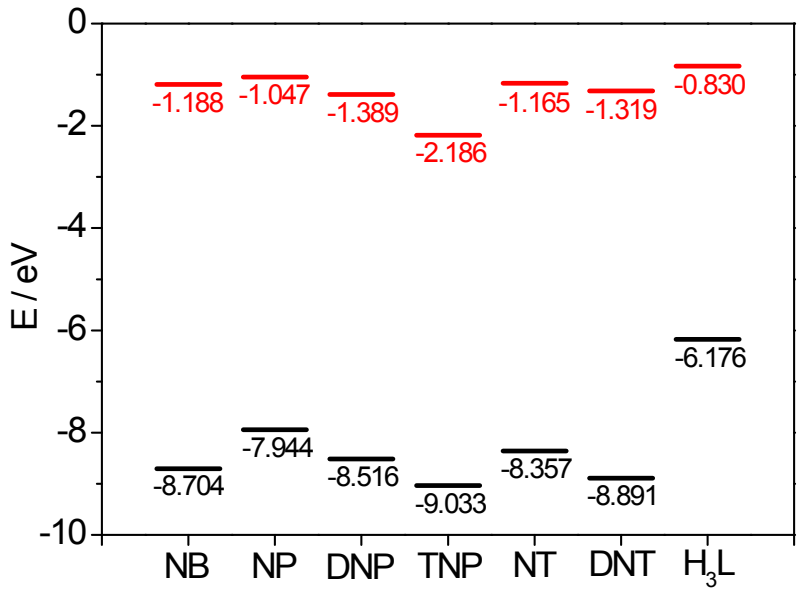

Fig. S18. Relative energies of ligands and NACs, as calculated by using M06-2X/6-31G** level with the SMD solvation model.

Table S1. The frontier molecular orbital energies for ligands and NACs as calculated at M06-2X/6-31G** level of theory.

	HOMO / eV	LUMO / eV	Energy Gap / eV
NB	-8.704	-1.188	7.516
NP	-7.944	-1.047	6.897
DNP	-8.516	-1.389	7.127
TNP	-9.033	-2.186	6.847
NT	-8.357	-1.165	7.192
DNT	-8.891	-1.319	7.572
H_3L	-6.176	-0.830	5.346

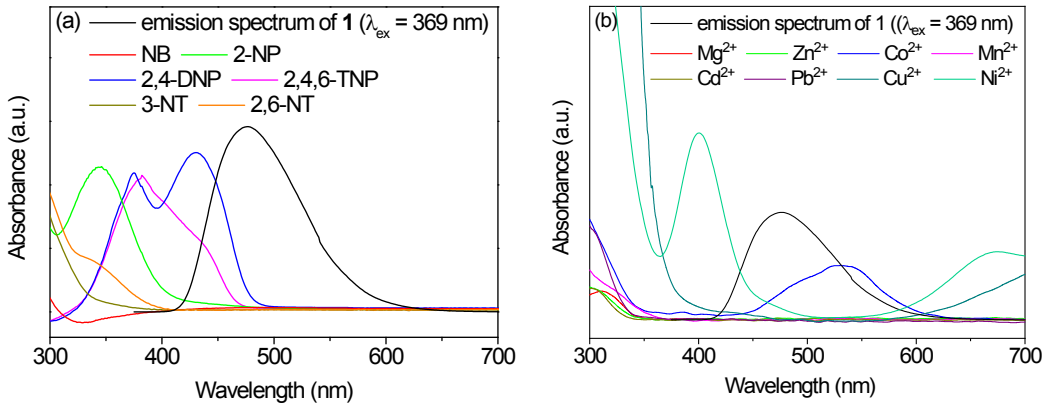

Fig. S19. UV-Vis absorption spectra of (a) nitroaromatic molecules, (b) metal ions in DEF and the emission spectrum of **1**.

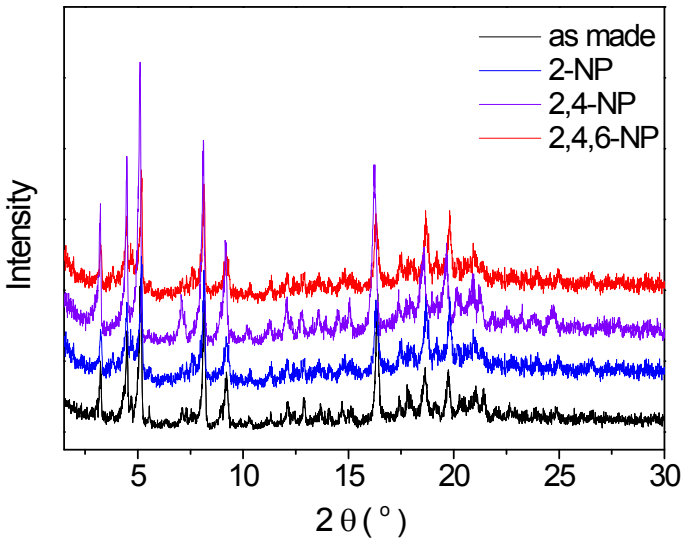

Fig. S20. PXRD profiles of **1** after quenching studies for NB, NP, DNP, and TNP.

After the PL experiments, the dispersed solutions of complex **1**-nitroaromatic compounds were centrifuged and washed with fresh DEF. The centrifugation and washing step were repeated five times and then immersed in fresh DEF with stirring for 1 h. After that, the supernatant was decanted. The solid product **1** was dried under N_2 atmosphere and then PXRD was collected.

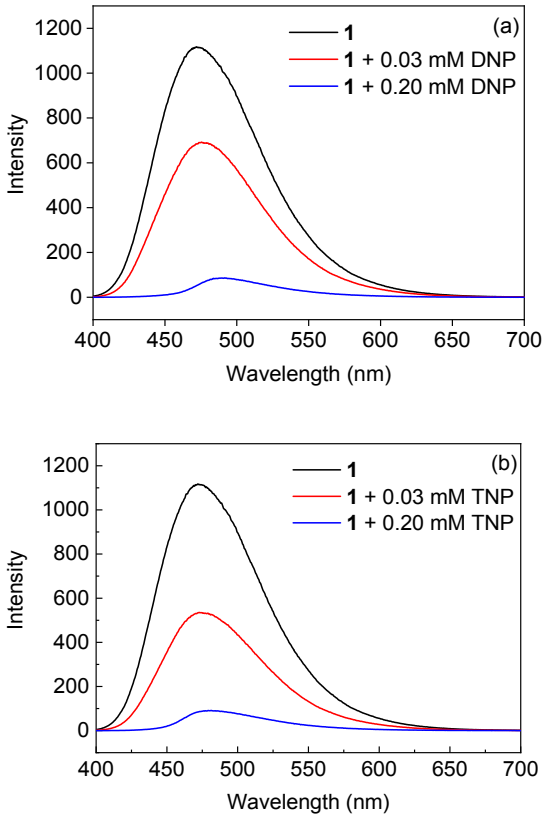

Fig. S21. Emission spectra of **1** upon increasing addition of various concentration of (a) DNP and (b) TNP.

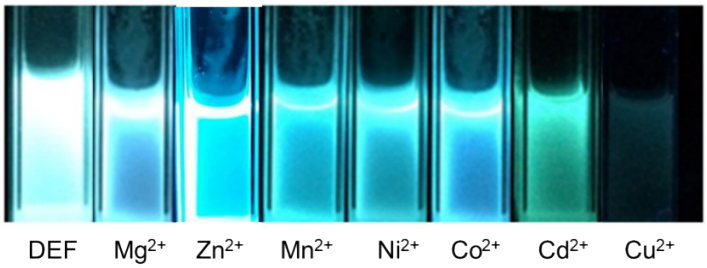

(a)

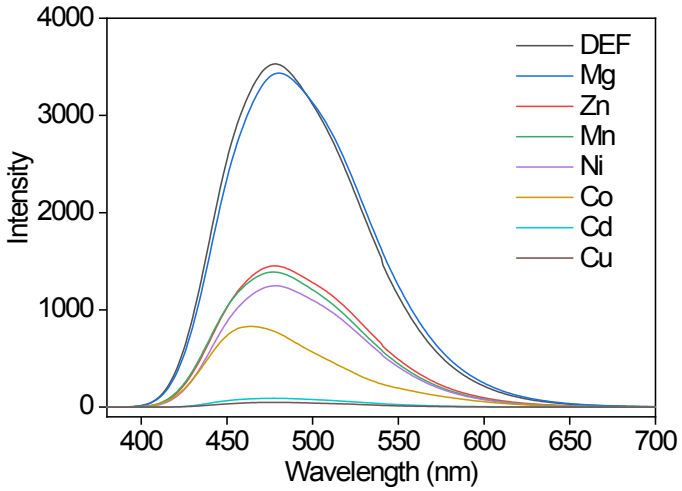

(b)

Fig. S22. (a) Photographs of **1** dispersed in DEF with the indicated metal ions after UV irradiation. (b) Photoluminescence data of **1** after addition of metal ions in DEF.

Table S2. Calculated values of quenching effect coefficients (K_{SV}).

Metal ions	Ksv [M^{-1}]
Mn^{2+}	26.53
Mg^{2+}	3.91
Ni^{2+}	80.83
Co^{2+}	85.4
Cd^{2+}	1489.36
Cu^{2+}	1608.67

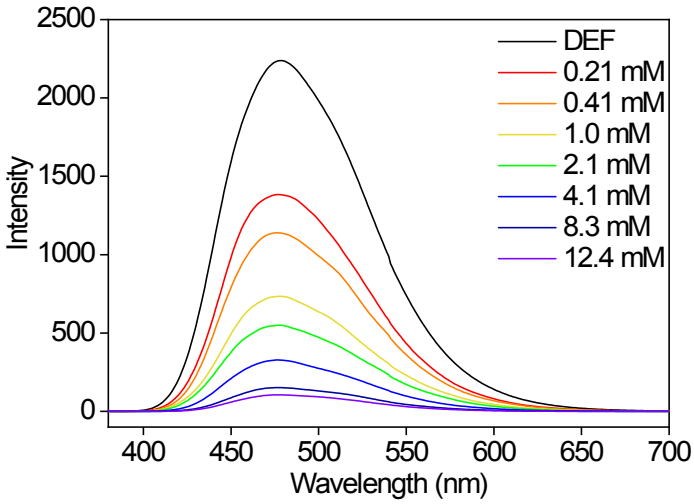

Fig. S23. Photoluminescence data of **1** after addition of Cu^{2+} solution with different concentrations.

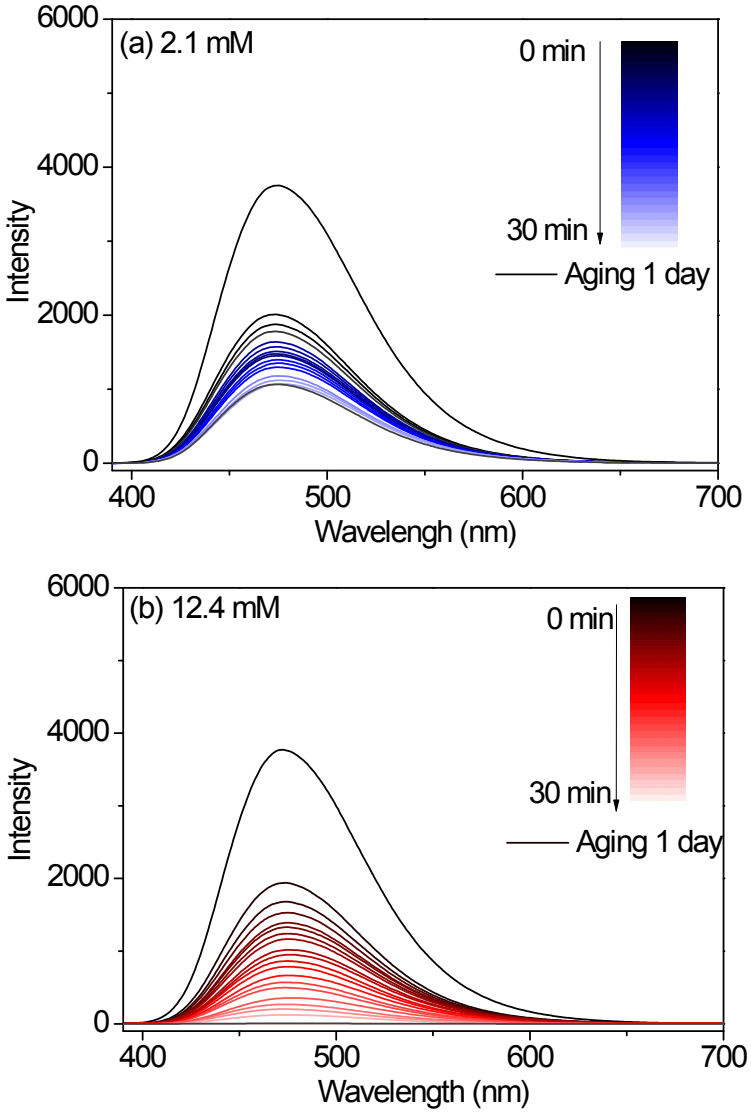

Fig. S24. Time-dependence fluorescence intensity variation in (a) 2.1 mM and (b) 12.4 mM Cu^{2+} solutions.

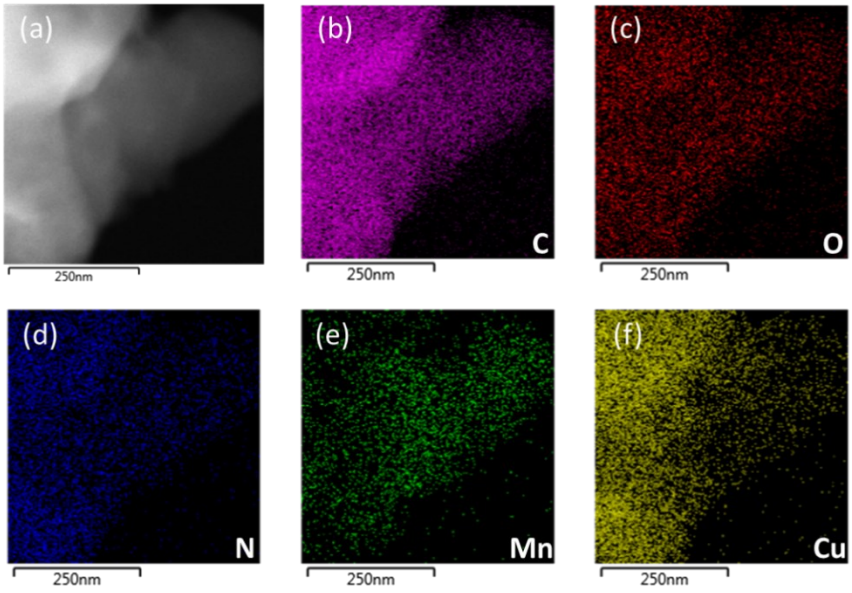

Fig. S25. (a) TEM-EDS image of Cu^{2+}-incorporated **1,** TEM-EDS elemental mapping images of (b) C, (c) O, (d) N, (e) Mn, and (f) Cu in Cu^{2+}-incorporated **1**, indicating that diffusion of Cu^{2+} ions into the pores of the framework.

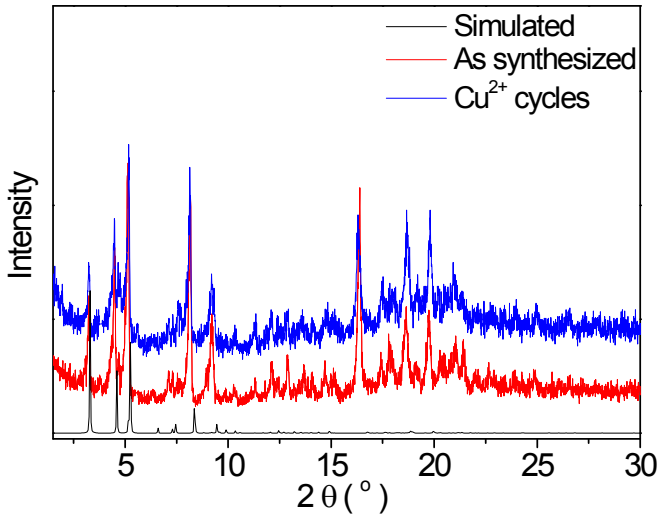

Fig. S26. PXRD data of **1** (red) before and (blue) after 5 cycles. The black line stands for the simulated pattern.

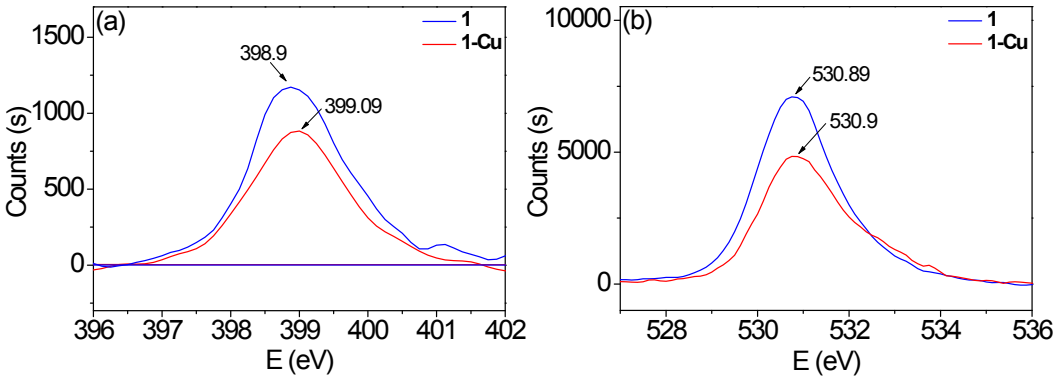

Fig. S27. (a) N1s and (b) O1s peaks in the XPS spectra of **1** and **1-Cu**.

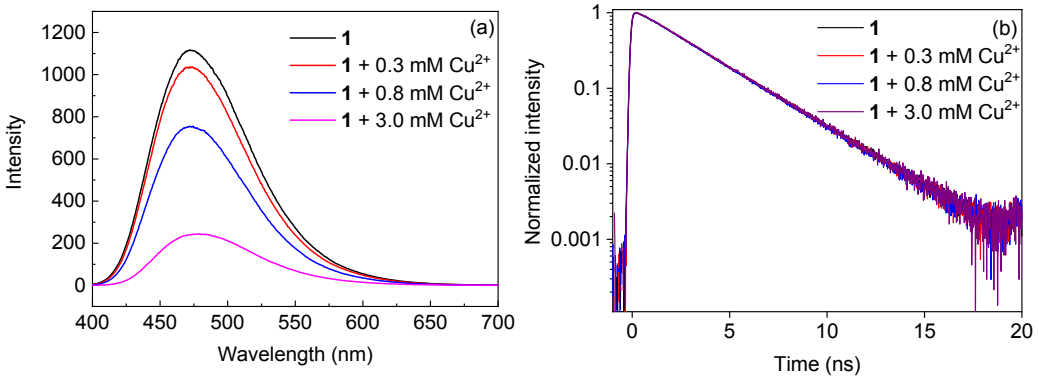

Fig. S28. (a) Emission spectra and (b) TRF signals of **1** upon increasing addition of various concentration of Cu^{2+} solution. Excitation wavelength is 375 nm.

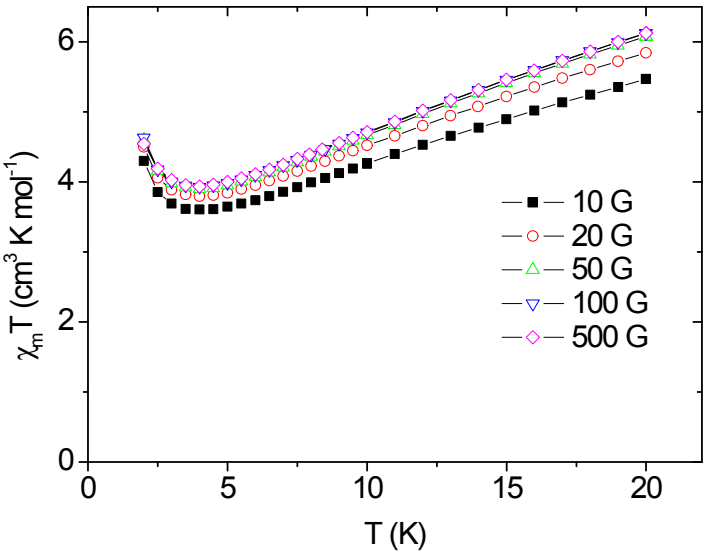

Fig. S29. Plots of $\chi_m T$ versus *T* for **1** at several magnetic fields.

The molar susceptibility can be derived from the general form of the Van Vleck equation. The general expression of magnetic susceptibility for the Mn_3 trimer (S_{Mn} = 5/2) is given as below.

$p = J_t/kT$

A =

52.5+15exp(2.5p)+126exp(3.5p)+52.5exp(5p)+1.5exp(5p)+15exp(6.5p)+1.5exp(8p)+247.5exp(8p)
+126exp(8.5p)+52.5exp(9p)+15exp(9.5p)+15exp(11.5p)+52.5exp(12p)+126exp(12.5p)+247.5exp(13p)
+429exp(13.5p)+52.5exp(14p)+52.5exp(15p)+126exp(15.5p)+247.5exp(17p)+126exp(17.5p)
+429exp(18.5p)+247.5exp(20p)+682.5exp(20p)+429exp(22.5p)+682.5exp(25p)+1020exp(27.5p)

B =

6+4exp(2.5p)+8exp(3.5p)+6exp(5p)+2exp(5p)+4exp(6.5p)+2exp(8p)+10exp(8p)+8exp(8.5p)
+6exp(9p)+4exp(9.5p)+4exp(11.5p)+6exp(12p)+8exp(12.5p)+10exp(13p)+12exp(13.5p)+6exp(14p)
+6exp(15p)+8exp(15.5p)+10exp(17p)+8exp(17.5p)+12exp(18.5p)+10exp(20p)+14exp(20p)
+12exp(22.5p)+14exp(25p)+16exp(27.5p)

$\chi_m(\text{trimer}) = (Ng^2\beta^2/3kT)(A/B)$

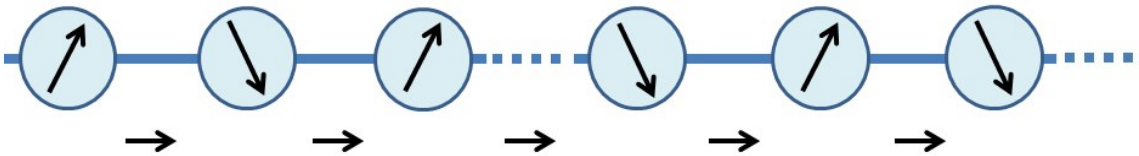

Fig. S30. Spin canting phenomenon in the antiferromagnetically coupled chain. Weak ferromagnetism occurs as a result of the canted spin system.

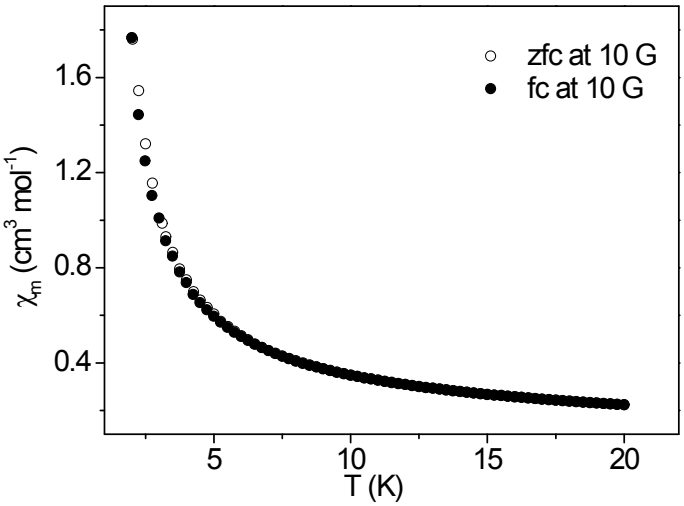

Fig. S31. Plots of zero-field cooled (zfc) and field-cooled (fc) magnetization curves for **1** at 10 G.

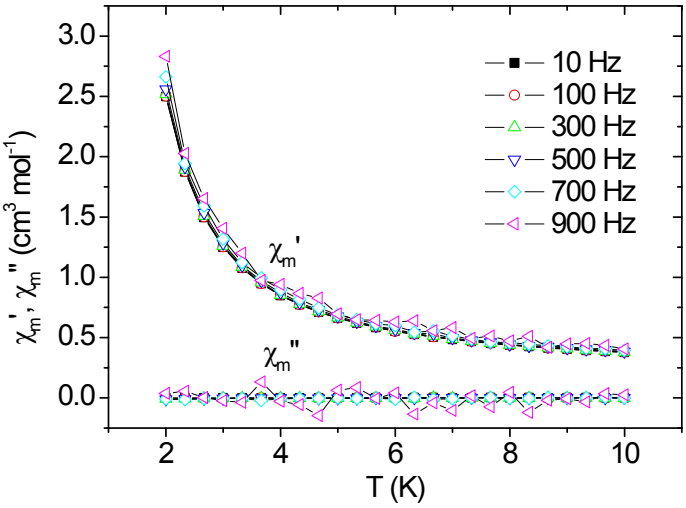

Fig. S32. Plots of χ_m' and χ_m" versus *T* for **1** at the indicated frequencies.